

1 **Nanoscopic resolution within a single imaging frame**

2 Esley Torres García ^{1,2}, Raúl Pinto Cámara ^{1,2}, Alejandro Linares ², Damián Martínez ², Víctor Abonza ²,
3 Eduardo Brito-Alarcón ², Carlos Calcines-Cruz ³, Gustavo Valdés-Galindo ⁴, David Torres ², Martina
4 Jabłoński ⁵, Héctor H. Torres-Martínez ⁶, José L. Martínez ⁷, Haydee O. Hernández ⁸, José P. Ocelotl-
5 Oviedo ², Yasel Garcés ^{2,7}, Marco Barchi ⁹, Joseph G. Dubrovsky ⁶, Alberto Darszon ⁷, Mariano G.
6 Buffone ⁵, Roberto Rodríguez Morales ¹⁰, Juan Manuel Rendon-Mancha ¹ Christopher D. Wood ²,
7 Armando Hernández-García ⁴, Diego Krapf ¹¹, Álvaro H. Crevenna ¹², and Adán Guerrero ^{2,*}.

8

9 ¹ Centro de Investigación en Ciencias, Instituto de Investigación en Ciencias Básicas y Aplicadas,
10 Universidad Autónoma del Estado de Morelos, Cuernavaca, Morelos, Mexico.

11 ² Laboratorio Nacional de Microscopía Avanzada, Instituto de Biotecnología, Universidad Nacional
12 Autónoma de México, Cuernavaca, Morelos, Mexico.

13 ³ Instituto de Investigaciones Biomédicas, Universidad Nacional Autónoma de México. Ciudad de
14 México, Mexico.

15 ⁴ Departamento de Química de Biomacromoléculas, Instituto de Química. Universidad Nacional
16 Autónoma de México. Ciudad de México, Mexico.

17 ⁵ Instituto de Biología y Medicina Experimental (IBYME-CONICET), Buenos Aires, Argentina.

18 ⁶ Departamento de Biología Molecular de Plantas, Instituto de Biotecnología, Universidad Nacional
19 Autónoma de México, Cuernavaca, Mexico.

20 ⁷ Departamento de Genética del Desarrollo y Fisiología Molecular, Instituto de Biotecnología,
21 Universidad Nacional Autónoma de México, Cuernavaca, Morelos, Mexico.

22 ⁸ Instituto de Investigaciones en Matemáticas Aplicadas y en Sistemas, Universidad Nacional Autónoma
23 de México, Ciudad de México, Mexico.

24 ⁹ Department of Biomedicine and Prevention, Faculty of Medicine, University of Rome Tor Vergata,
25 Rome, Italy.

26 ¹⁰ Instituto de Cibernética, Matemática y Física, Ciudad de la Habana, Cuba.

27 ¹¹ Electrical and Computer Engineering and School of Biomedical Engineering, Colorado State
28 University, Fort Collins, Colorado 80523, U.S.A.

29 ¹² European Molecular Biology Laboratory, Neurobiology and Epigenetics Unit, Monterotondo, Italy.

30

31 * Correspondence contact: adan.guerrero@ibt.unam.mx

32 **Abstract**

33 Mean-Shift Super Resolution (MSSR) is a principle based on the Mean Shift theory that
34 improves the spatial resolution in fluorescence images beyond the diffraction limit.

35 MSSR works on low- and high-density fluorophore images, is not limited by the
36 architecture of the detector (EM-CCD, sCMOS, or photomultiplier-based laser scanning
37 systems) and is applicable to single images as well as temporal series. The theoretical
38 limit of spatial resolution, based on optimized real-world imaging conditions and
39 analysis of temporal image series, has been measured to be 40 nm. Furthermore, MSSR
40 has denoising capabilities that outperform other analytical super resolution image
41 approaches. Altogether, MSSR is a powerful, flexible, and generic tool for
42 multidimensional and live cell imaging applications.

43

44 **Key Words:** super-resolution microscopy, diffraction limit, single frame, Mean Shift,
45 fluorescence microscopy, live-cell imaging.

46

47 **Introduction**

48 Super-resolution Microscopy (SRM), which encompasses a collection of
49 methods that circumvent Abbe's optical resolution limit, has dramatically increased our
50 capability to visualize the architecture of cells and tissues at the molecular level. There
51 are several approaches to SRM which vary in terms of the final attainable spatial and
52 temporal resolution, photon efficiency, as well as in their capacity to image live or fixed
53 samples at depth [1, 2]. One class of techniques exceed the diffraction limit by
54 engineering the illumination or the point spread function (PSF), such as SIM and STED
55 [3-5]. These techniques can be used for live imaging although they require specialized
56 hardware and dedicated personnel for maintenance and operation. Single-molecule
57 localization methods (e.g., STORM, PAINT, PALM) [6-9] that localize individual
58 emitters with nanometer precision require temporal analysis of several hundred-to-
59 thousands of images and are prone to error due to fast molecular dynamics within live
60 specimens.

61 Some SRM computational methods have few or no demands on hardware or
62 sample preparation and provide resolution improvements beyond the diffraction limit
63 [10-13]. The quantity and performance of computational methods have both increased
64 over the past decade given the many advantages they present, such as their low barriers
65 to entry and generic applicability to data acquired with any microscopy modality (wide-

66 field, confocal, or light-sheet). However, these methods also present some limitations,
67 such as the possible introduction of artifacts [14], the requirement for high signal-to-
68 noise ratio (SNR) data and the acquisition of tens to hundreds of frames [10-13], which
69 limit their applicability to reconstruct fast dynamical processes.

70 Here, we introduce the Mean Shift Super-Resolution principle for digital images
71 ‘MSSR’ (pronounced as *messer*), derived from the Mean Shift (MS) theory [15, 16].
72 MSSR improves the resolution of any single fluorescence image up to 1.6 times,
73 including its use as a resolution enhancement complement after the application of other
74 super-resolution methods. Additionally, we demonstrate the super-resolving capabilities
75 of MSSR as a standalone method for a variety of fluorescence microscopy applications,
76 through a single-frame and temporal stack analysis, allowing resolution improvements
77 towards a limit of 40 nm.

78 Open-source implementations of MSSR are provided for ImageJ (as a plugin),
79 R, and MATLAB, some of which take advantage of the parallel computing capabilities
80 of regular desktop computers (Supplementary Note 7). The method operates almost free
81 of parameters; users only need to provide an estimate of the point spread function (PSF,
82 in pixels) of the optical system, choose the MSSR order, and decide whether a temporal
83 analysis will take place (Supplementary material MSSR Manual). The provided open-
84 source implementations of MSSR represent a novel user-friendly alternative for the
85 bioimaging community for unveiling life at its nanoscopic level.

86

87 **Results**

88 *The MSSR principle.*

89 MSSR is tailored around the assumption that fluorescence images are formed by
90 signals collected from point sources (i.e., fluorophores) convolved with the PSF of the
91 microscope (Supplementary Notes 1, 2 and 3). Processing a single image with MSSR
92 starts with the calculation of the MS, which guarantees that large intensity values on the
93 diffraction-limited (DL) image coincide with large positive values in the MSSR image
94 (Supplementary Note 4). Further algebraic transformations then restore the raw intensity
95 distribution and remove possible artifacts caused by the previous step (edge effects and
96 noise dependent artifacts), giving rise to an image that contains objects with a narrower
97 full width at half maximum (FWHM) (Figure 1a). This procedure is denoted by MSSR⁰,
98 as the first stage to shrink emitter distribution.

99 The MS is locally computed by a kernel window that slides throughout the entire
100 image, subtracts the sample mean (weighted local mean) as well as the central value of
101 the kernel using a spatial-range neighborhood (Supplementary Notes 2 and 3, Figure S4
102 and S5, Table S1) [15, 16]. The MS is a vector that always points towards the direction
103 of the intensity gradient and its length provides a local measure of the fluorescence
104 density and brightness [17-19]. Since the MS lies within the gradient space, its values
105 depend on the difference between the central pixel of the neighborhood and the
106 surrounding pixels and thus is not necessarily linked to the fluorescence intensity values
107 of the raw image. A mathematical proof, provided in Supplementary Note 4,
108 demonstrates that the minimum MS value, computed from a Gaussian distribution,
109 matches with the point of maximum intensity of the initial distribution (Supplementary
110 Note 4, Figure S6).

111 The increase in resolution offered by $MSSR^0$ was evaluated by the Rayleigh and
112 Sparrow limits [20-22], which are two criteria that establish resolution bounds for two
113 near-point sources (Figure 1b). Processing with $MSSR^0$ of two-point sources located at
114 their resolution limit (2.5σ and 2σ for Rayleigh and Sparrow limit respectively, Figure
115 1c vertical discontinuous lines) decreases the dip (height at the saddle point) [23] within
116 their intensity distributions (Figure 1b and 1c). Processing a single image with $MSSR^0$
117 shifts the resolution limit by 26 % and 20 %, according to the Rayleigh and Sparrow
118 limits respectively (Figure 1c vertical continuous lines). Therefore, processing a single
119 fluorescence image with $MSSR^0$ will reduce the FWHM of individual emitters. Also, a
120 comparison of the shrinkability of $MSSR^0$ applied to Gaussian and Bessel distributions
121 are shown in Figure S7. Additionally, the reduction of FWHM of Bessel distribution at
122 different wavelengths of the visible spectrum are shown in Figure S8.

123 Since the result of $MSSR$ is an image, we used the resulting image to seed an
124 iterative process (Figure 2a). We refer to this as higher-order $MSSR$ ($MSSR^n$, $n>0$),
125 which delivers a further gain of resolution per n -iteration step (Figures. 2a and S9). As
126 the order of $MSSR^n$ increases, both the FWHM of emitters (Figure S10) and the dip of
127 their intensity distribution decrease (Figure 2b). Numerical approximations indicate that
128 two point-sources separated at 1.6σ are resolvable with $MSSR^3$, but not when their
129 separation is 1.5σ (Figure 2b). The separation of 1.6σ sets the theoretical resolution
130 limit of $MSSR^n$.

131 To empirically test the ability of MSSRⁿ to achieve super-resolution image
132 within a single frame, a commercial nanoruler sample (GATTA-SIM140B,
133 GATTAquant) was imaged by Structured Illumination Microscopy (SIM) and widefield
134 fluorescence microscopy, which was then processed by MSSRⁿ. The iterative
135 processing of the widefield data with MSSR³ reveals the two fluorescence emitters
136 located at a separation of 140 nm which is consistent with the result obtained by SIM
137 (Figure 2c).

138

139 *MSSR further increases the resolution of super-resolved images.*

140 Based on the MSSR capabilities to generate a super-resolved micrograph after
141 processing a single fluorescence image, we explored if a pre-existing super-resolved
142 image can be further enhanced by MSSR.

143 First, we used temporal stack of DL images of tubulin-labeled microtubules
144 collected at high fluorophore density [24] (previously used to test and compare a variety
145 of SRM algorithms) [25], which were subject to ESI, SRRF or MUSICAL analysis [11-
146 13], where each was used to compute a single super-resolved image (Figure 3a).
147 Supplementary note 9 contains an in-depth comparison of MSSR reconstructions
148 combined with other SRM analytical methods (ESI, SRRF and MUSICAL), which
149 achieve super-resolution through a temporal analysis [12-14]. Post-processing of ESI,
150 SRRF or MUSICAL images with MSSR⁰ increases contrast and resolution (Figure 3a).

151 Second, a sequence of images of randomly blinking emitters placed along a
152 synthetic tubular structure [26] was processed with MSSR⁰ after analysis with
153 MUSICAL. In both reconstructions, three regions (small squares in Figure 3b) were
154 chosen to assess the gain in resolution, visualized in terms of the distance between the
155 normalized intensity distributions peaks. MSSR further resolves the edges of the
156 synthetic structures on the MUSICAL-processed image without changing the position
157 of the distribution peaks (Figure 3b) as predicted by our theory.

158 Lastly, we applied MSSR on a super-resolved SIM image of sister chromatids of
159 mouse chromosomes (Figure 3c). Similar to the results obtained above, processing with
160 MSSR increases both the contrast and resolution of the final image. Each of the
161 individual SRM methods tested performs optimally under specific experimental

162 conditions; one can thus choose whichever of them to use based on the available
163 infrastructure, optical setup, and biological or experimental conditions that best fit the
164 specific research goals. Altogether these data show that post-processing with MSSR
165 increases resolution by a factor up to 1.6 times of any tested super-resolution technique.

166 *Temporal analysis of MSSR*

167 In theory, MSSR can be applied to a sequence of images (Supplementary Note
168 5). Based on the increase in resolution offered by computational methods that rely on
169 temporal analyses (SRRF, ESI, MUSICAL), we investigated whether a further
170 resolution gain could be achieved by applying a temporal analysis to a sequence of
171 single frame MSSR images (t-MSSRⁿ) (Figure 4a). Pixel-wise temporal functions
172 (*PTF*), such as average (*Mean*), variance (*Var*), the temporal product mean (*TPM*),
173 coefficient of variation (*CV*) or auto-cumulant function of orders 2 to 4 (*SOFI*₂, *SOFI*₃,
174 *SOFI*₄) [10], can be used to create an image with enhanced spatial resolution
175 (Supplementary Note 5, Table S2).

176 To experimentally validate the increase in resolution from single-frame (sf-
177 MSSRⁿ) to t-MSSRⁿ, we used two different nanoruler systems, an in-lab CRISPR/
178 dCas12a nanoruler, used to score nanoscopic distances between individual fluorescent
179 sites down to 100 nm, and a commercial nanoruler with fluorophores positioned at 40
180 nm of separation (GATTA-PAINT, 40G, and 40RY. Gattaquant).

181 The CRISPR/dCas12a nanoruler system consists of a dsDNA with four binding
182 sites for dCas12a uniformly distributed every 297 bp (equivalent to ~ 100 nm of
183 separation) (Figure S33a). To validate this system, we imaged the association of the
184 CRISPR/dCas12a complex to the binding sites on the dsDNA by atomic force
185 microscopy (AFM) and measured the distance between each dCas12a complex (Figure
186 S33b).

187 The CRISPR-dCas12a nanorulers were then imaged in buffer by total internal
188 reflection fluorescence microscopy (TIRFM) for further MSSR analysis. We used a
189 DNA-PAINT approach for fluorescence indirect tagging [27], in which a fluorescent
190 ssDNA probe hybridizes with an extension of the gRNA. The “blinking” of the
191 fluorescence signal is attained by events of association and dissociation between the
192 fluorescent probe and the gRNA on the CRISPR/dCas12a nanoruler at the binding site.

193 In the DL image, amorphous spot-like fluorescent patterns were observed
194 (Figure 4b). sf-MSSR³ processing of either an isolated frame or an average projection of
195 the corresponding stack of 100 images (DL-AVG) could not resolve individual
196 CRISPR/dCas12a binding sites (Figure 4b), and only after processing by t-MSSR³ did
197 individual binding sites become resolved (Figure 4c). The result of t-MSSR³ varied in
198 relation to the temporal function used (Figure 4c). The best result for this nanoruler was
199 obtained by the pixel-wise temporal variance (*Var*) of the sf-MSSR³ stack (Figure 4c). t-
200 MSSR³-*Var* resolved nearby emitters engineered to recognize binding sites located at
201 100 nm (Supplementary Movie S1), provided by scoring association-dissociation events
202 between the imaging probe and the gRNA.

203 To determine the distance between two dCas12a sites along the DNA chain we
204 obtained the distribution of distances between dCas12a binding sites taking in
205 consideration their unidimensional association to a semi-flexible polymer such as the
206 DNA [28]. Estimated distances after t-MSSR³-*Var* in the CRISPR/dCas12a nanoruler
207 are 85 ± 14 nm, 152 ± 21 nm, 232 ± 37 nm (Figure 4d). These results confirm that t-
208 MSSR³ can successfully resolve nanoscopic distances.

209 To explore the resolution limit attainable by t-MSSRⁿ even further, we looked at
210 a nanoruler system with smaller separation between fluorophore sites (from Gattaquant)
211 (Figure S34a). Analysis with t-MSSR³ of 100 images revealed individual fluorescent
212 spots at 40 nm apart (Figure 4e and Supplementary Figure S34b). The data presented in
213 Figure 4e demonstrate that t-MSSR³ resolves nanoscopic distances in the 30-80 nm
214 range, validating a lower experimental spatial resolution bound of 0.5σ (≈ 40 nm),
215 which depends on the emission wavelength of the fluorophore (Figure 4e,
216 Supplementary Figure S8c). In comparison, SRRF, ESI and MUSICAL were not able to
217 resolve fluorescent emitters located 40 nm apart, consistent with their limit within the
218 range of 50–70 nm (Figure 4f) [11-13].

219

220 *Single frame nanoscopy, free of noise-dependent artifacts*

221 The theory of image processing by MSSR (Supplementary Note 5), suggests that
222 it should be robust over a wide range of SNR, granted by four factors. First, when
223 processing a single frame, MS works as a local spatial frequency filter (a smoothing
224 filter); regions corresponding to the image background are homogenized by the kernel
225 window, reducing variation in background noise. Second, one of the steps of the MSSR

226 procedure is to remove the MS negative constraints. This threshold operation exerts
227 influence on structures at σ , at about 65% of the intensity distribution of the emitters;
228 values below this threshold will be considered as noise and set to zero value. Third,
229 when using a PTF, nanoscopic information is enriched due to temporal oversampling of
230 the hidden fluorescent structure. Fourth, the spatial kernel of the MSSR algorithm
231 operates within the subpixel realm; the number of neighboring pixels is digitally
232 increased through bicubic interpolation providing digital oversampling of the emitters'
233 locations (Supplementary Note 6).

234 We then experimentally assessed the capacity of MSSR to denoise fluorescence
235 images and determine whether it introduces noise-related artifacts. We used a PSFcheck
236 slide [29], which contains an array of regular fluorescent nanoscopic patterns shaped by
237 laser lithography (Figure 5). Analysis with sf-MSSRⁿ or t-MSSRⁿ showed, in
238 comparison to alternative approaches, striking denoising capabilities without
239 introducing noticeable artifacts (Figure 5a) (Supplementary Note 9). These artifacts,
240 resembling amorphous nanoscopic structures around the fluorescent ring or within it,
241 were commonly found at reconstructions generated by other analytical techniques
242 (Figure S22).

243 Starting at a SNR > 2, sf-MSSR¹ provides reliable SRM reconstructions of
244 comparable quality to other SRM approaches, which demand the temporal analysis of
245 the fluorescence dynamics (Figure 5a and Supplementary Note 9). We quantified the
246 quality of the reconstructions by calculating the Resolution Scaled Pearson (RSP)
247 coefficient and the Resolution Scaled Error (RSE), which provide a global measurement
248 of the quality of the reconstruction by comparing the super-resolution image and the
249 reference image (in this case, the DL image) [14]. Higher RSP and lower RSE values
250 are associated with reliable reconstructions (Supplementary Note 8). When the SNR is
251 above 5, all tested algorithms perform similarly well in quality (Figure 5b), but their
252 global errors differ from each other (Figure 5c). As expected, the RSE increased as a
253 function of the SNR of the input images for any tested algorithm (Figure 5c).

254 Furthermore, the performance of MSSR in achieving a satisfactory
255 reconstruction was assessed by varying the number of input images using a temporal
256 analysis scheme (Supplementary Note 8). With SNR > 2 input data, RSP reaches near
257 maxima values and RSE near minima values when processing a single frame (Figure
258 S19-20, Supplementary Movie S2). However, when computing MSSR using low SNR

259 input data (SNR \sim 2) a temporal analysis is required as RSP and RSE values reach a
260 plateau only when a temporal stack of as few as 20 images is used (Figure S20-21,
261 Supplementary Movie S3). These findings illustrate that the minimal number of frames
262 needed by MSSR to provide a reliable reconstruction depends on the information itself,
263 i.e., on the SNR and on the photophysical properties of the specimen (movies S1 - S3);
264 and can be determined by computing RSP and RSE as function of the number of
265 analyzed frames with t-MSSRⁿ (Figure S21).

266

267 *Nanoscopic resolution with conventional fluorescence imaging*

268 To showcase the versatility of MSSR to super-resolve data acquired from
269 different fluorescence applications, we evaluated its performance over a collection of
270 experimental scenarios (Supplementary Note 10).

271 Analysis with MSSR provided nanoscopic resolution of rotavirus replication
272 machineries (Figure S25), which were recently described by Garcés *et al* as a layered
273 array of viral protein distributions [30]. Originally, it took the authors several days to
274 weeks to generate a single super-resolution image by means of analyzing several stacks
275 of hundreds of DL images using 3B-ODE SRM. With MSSR, we were able to achieve
276 comparable results, through analyzing single DL frames within seconds with a regular
277 desktop computer with either sf-MSSR¹ or t-MSSR¹ (Supplementary Note 7).

278 Mouse sperm cells are used to study the acrosomal exocytosis (AE), a unique
279 secretory process which results from fusion events between the plasma membrane and a
280 specialized vesicle called acrosome located in the sperm head [31,32]. Nanoscopic
281 remodeling of both plasma membrane and actin cytoskeleton was imaged during the AE
282 by means of sf-MSSR¹, showing single frame temporal resolution (of milliseconds)
283 (Figs. S26). At the onset of the AE, the FM4-64 fluorescence (a probe that fluoresces
284 when bound to membranes) was confined to the plasma membrane and was visible
285 above of a F-actin cytoskeleton fringe. During the AE, several fenestration events were
286 observed to occur at both the plasma and acrosome membranes, as consequence of that,
287 a notorious increase of FM4-64 was observed close-bellow the F-actin fringe
288 (Supplementary Movie S5 a-f). The AE is a dynamic remodeling process that takes
289 minutes to occur, sf-MSSR¹ allows the observation of events occurring at the
290 millisecond scales, which are hindered when using other SRM multi-frame analytical
291 approaches, such as SRRF or 3B [11, 33], due to their mandatory need of a temporal

292 analysis of the fluorescence dynamics to unveil nanoscopic detail (compare Figures S26
293 and S27).

294 Background noise is known to be an important issue in single-particle tracking
295 (SPT) applications as it decreases the ability to faithfully localize particles and follow
296 them through time [34, 35]. Moreover, the spatial overlap of PSFs derived from
297 individual particles makes it challenging for SPT algorithms to recognize them as
298 separate entities. The denoising capabilities of sf-MSSR¹ enhanced both the contrast and
299 spatial resolution of freely diffusing in-silico particles previously used as benchmarks to
300 test a variety of SPT algorithms (Figure S28) [36]. Pre-processing of the images with sf-
301 MSSR¹ improved the tracking performance of three commonly employed SPT tracking
302 algorithms: (i) the LAP framework for Brownian motion as in [37, 38], (ii) a linear
303 motion tracker based on Kalman filter [39-41], and (iii) a tracker based on Nearest
304 neighbors [42-44] within a wide range of particle densities and SNR (Figure S29).
305 Additional testing with sf-MSSRⁿ showed an increase in nanoscopic colocalization
306 accuracy in double imaging experiments in single-molecule DNA curtain assays (Figure
307 S30) [45].

308 Plasmalemma- and nuclear-labeled transgenic *Arabidopsis thaliana* plants are
309 routinely used to study cell fate and proliferation during root development in time-lapse
310 confocal microscopy experiments in two and three dimensions [46, 47]. When applied
311 to lateral root primordium cells, located deep inside the parent root, sf-MSSR¹
312 demonstrated the capacity to achieve multidimensional nanoscopic resolution as it
313 revealed isolated nanodomains resembling nucleosome clutches, previously reported in
314 mammalian cells [48, 49], within the nuclei of a lateral root primordium cells (Figure
315 S31 and Supplementary Movie S10). Similar observations were performed upon
316 epidermal root tissues visualized via selective plane illumination microscopy (SPIM)
317 after examination of volumetric data with sf-MSSR¹ (Figure S32). In combination, these
318 studies provide evidence for the capabilities of MSSR to resolve biological detail at
319 nanoscopic scales using either simple or advanced fluorescence microscopy
320 technologies.

321

322

323

324 **Discussion**

325 *- Novel theoretical contributions*

326 From the historical point of view, since the seminal development of the MS
327 theory [15, 16] and until the present day, few statistical and imaging applications based
328 on the theory of MS compute the MS vector itself [50]. This can be explained, in part,
329 because previous applications of MS are based on finding modes in the features space
330 and did not operate directly in the derivative space. In contrast, MSSR represents an
331 application of MS theory that operates in the second derivative space. By computing the
332 MS vector and estimating densities among pixels, MSSR computes a probability
333 function for the fluorophore estimates whose individual fluorescence distributions are
334 narrowed in comparison with the PSF of the optical system. The exploration of the
335 information stored on the second derivative space of the image can be also achieved by
336 substituting the MS by similar functions that operate in such space, e.g., Laplacian,
337 Hessian, Difference of Gaussians [51] which, in comparison with the MS, offer
338 computational advantages as they can be expressed in the Fourier space and
339 implemented using the FFT algorithm [51]. The information harbored in the second
340 derivative space of the DL image is used by MSSR to compute a super-resolved image
341 with higher spatial frequencies than the corresponding DL image, hence, overcoming
342 both the Rayleigh and Sparrow limits, and setting up an undescribed limit of resolution
343 which deserves further exploration and characterization.

344 The MS theory is not restricted by the number of dimensions of the information
345 required to compute the kernel windows over which MSSR operates (Supplementary
346 notes 2 and 3). Given that, MSSR parameters are suitable to extend its application to
347 assess data with higher dimensions. For example, in 2D images, the spatial parameter of
348 MSSR, which encompasses the lateral resolution width of the PSF, is defined to be the
349 same in the x and y dimensions of the image. In such case, the shape of the kernel is
350 circle- or square-like, depending on the application used. For three-dimensional (3D)
351 microscopy imaging, the lateral (x-y plane) and axial (x-z and y-z planes) dimensions
352 are affected in different ways by diffraction. The MSSR principle can be further
353 extended for explicit volumetric imaging by means of using an asymmetric kernel
354 which can be defined following the 3D lateral-axial aspect ratio of the PSF. In addition,
355 the definition of the spatial kernel can be refined to also consider possible deformations
356 of axial symmetry of the PSF due to optical aberrations introduced by the imaging

357 system or by the sample itself. A similar reasoning aimed to extend the portfolio of
358 applications of MSSR can be envisaged considering spatial-range parameter, the latter
359 narrowing down the working intensity space where local calculations of MSSR take
360 place.

361 *Novel contributions to microscopy*

362 We present a new SRM approach capable of achieving multidimensional nanoscopy
363 through single-frame analysis under low SNR conditions and with minimal noise-
364 dependent artifacts. Limited only by the imaging speed of the optical system setup,
365 MSSR increases resolution by analyzing either a single frame, or by applying MSSR to
366 each individual image in a stack followed by the application of a pixel-wise temporal
367 function. MSSR is a powerful stand-alone method for either single or multi-frame SRM
368 approaches, or as post-processing method which can be applied to other analytical
369 multi-frame (restricted to camera-based systems) or hardware dependent SRM methods
370 for further enhancement of resolution and contrast. We demonstrated MSSR
371 compatibility with other SRM methods and showed that its usage improved resolution
372 and overall image quality in all the cases tested.

373 SRM analytical multi-frame approaches such as SRRF, ESI, MUSICAL and 3B
374 demand a temporal analysis which limits their utility for multi-dimensional imaging of
375 live samples [46]. The need to collect hundreds to thousands of images of the same
376 pseudo-static scene, challenges the applicability of these methods in multidimensional
377 imaging. The temporal multi-frame requirement imposes a tradeoff between the
378 achievable temporal and spatial resolutions. MSSR removes these constraints while
379 maintaining computational efficiency (Supplementary note 7).

380 We present applications of the MSSR principle that revealed fast molecular
381 dynamics through single-frame analysis of live-cell imaging data, with reduced
382 processing times in comparison with similar SRM approaches (Supplementary notes 7
383 and 10). Moreover, MSSR greatly improves the tracking efficacy of SPT methods by
384 means of reducing background noise and increasing both the contrast and SNR of noisy
385 SPT movies, enhancing the ability to resolve the position of single emitters. MSSR
386 further pushes the limits of live-cell nanoscopy by its excellent single-frame
387 performance. This flexibility extends its utility to most fluorescence microscopy and
388 alternative SRM methods.

389 Achieving both high (or sufficient) temporal and spatial resolution within a
390 broad range of fluorescence microscopy applications is a common goal among the
391 bioimaging community. With recent advances in microscopy equipment and imaging
392 protocols, the gap between the highest attainable resolution in the temporal and spatial
393 dimensions within the same experiment, has narrowed. This has been a challenge
394 especially because both parameters often involve mutually exclusive optical
395 instrumentation and experimental strategies. The introduction of MSSR represents one
396 more step in the right direction as it drastically reduces the amount of data needed to
397 reconstruct a single super-resolved micrograph.

398 No longer having to sacrifice either temporal or spatial resolution over the other,
399 has led some scientists to propose new ways to analyze imaging data. Some
400 approximations have been tailored to study millisecond molecular dynamics and
401 structural feature changes within the same experiment [52], e.g., by taking advantage of
402 the simultaneous use of image correlation spectroscopy (ICS) and SRM methods such
403 as SRRF [11]. In these contexts, MSSR could improve the analysis in three ways: a) it
404 delivers reliable SRM images in low SNR scenarios, which are common in the
405 experimental regimes of ICS due to the relatively fast frame rates of its applications, b)
406 MSSR introduces no noise-dependent artifacts which further refines the quality of the
407 spatial analysis and c) since no temporal binning is necessary for MSSR, there is no
408 restriction in the level of temporal detail retrievable from the ICS analysis.

409 Sub-millisecond time-lapse microscopy imaging can now be achieved by
410 sCMOS technologies, with applications for particle velocimetry [53], rheometry [54],
411 and optical patch clamp [55]. We envisage further applications for MSSR in these areas
412 through unveiling nanoscopic detail hidden in single DL images. Moreover, MSSR can
413 facilitate correlative nanoscopic imaging through crosstalk with other imaging
414 techniques such as electron microscopy, i.e., CLEM: correlative light electron
415 microscopy [56]; or atomic force microscopy, i.e., CLAFEM: Correlative light atomic
416 force electron microscopy [57]. In addition, MSSR can be applied to nanoscopic
417 volumetric imaging by using it together with expansion microscopy [58], oblique angle
418 microscopy [59], SPIM, and lattice light sheet microscopy [60], extending their
419 capabilities to previous unattainable resolution regimes.

420 A recent study by Chen R. et al., suggests that deep-learning based artificial
421 intelligence (AI) can reconstruct a super-resolution image from a single frame of a DL
422 image [61]. Such AI-based SRM approaches are promising, however, they are limited to

423 the existence of a maximum likelihood image obtained with another SRM, such as
424 STORM, that is required for neural network training an error minimization. Otherwise,
425 the method it is prompted to bias the final reconstruction toward the topological
426 information used to train the AI - network [61]. Our approach works completely
427 independent of other SRM methods and provides evidence of the existence of a new
428 resolution limit which lies on the second derivative space of the DL image, information
429 inaccessible when using neural networks.

430 MSSR applications might impact far beyond the field of microscopy, as its
431 principles can be applied to any lens-based system such as astronomy [62] and high-
432 resolution satellite imagery [63].

433

434 References

- 435 1 Galbraith, C. G. & Galbraith, J. A. Super-resolution microscopy at a glance, *J. cell*
436 *science*, **124**, 1607–1611, (2011).
- 437 2 Thorley, J. A., Pike, J. & Rappoport, J. Z. Chapter 14 - Super-resolution Microscopy: A
438 Comparison of Commercially Available Options. In Cornea, A. & Conn, P. M. (eds.)
439 *Fluorescence Microscopy*, 199–212, (Academic Press, Boston, 2014).
- 440 3 Hell, S. W. & Wichmann, J. Breaking the diffraction resolution limit by stimulated
441 emission: stimulated-emission-depletion fluorescence microscopy. *Opt. Lett.* **19**, 780–
442 782, (1994).
- 443 4 Gustafsson, M. G. Surpassing the lateral resolution limit by a factor of two using
444 structured illumination microscopy. *J. microscopy* **198**, 82–87, (2000).
- 445 5 Wegel, E. et al. Imaging cellular structures in super-resolution with SIM, STED and
446 Localisation Microscopy: A practical comparison. *Sci. Reports* **6**, 27290, (2016).
- 447 6 Betzig, E. et al. Imaging intracellular fluorescent proteins at nanometer resolution.
448 *Science* **313**, 1642–1645, (2006).
- 449 7 Bock, H. et al. Two-color far-field fluorescence nanoscopy based on photoswitchable
450 emitters. *Appl. Phys. B* **88**, 161–165, (2007).
- 451 8 Oi, C., Mochrie, S. G. J., Horrocks, M. H. & Regan, L. Paint using proteins: A new brush
452 for super-resolution artists. *Protein Sci.* **29**, 2142–2149, (2020).
- 453 9 Oi, C. et al. LIVE-PAINT allows super-resolution microscopy inside living cells using
454 reversible peptide-protein interactions. *Commun. Biol.* **3**, 458, (2020).
- 455 10 Dertinger, T., Colyer, R., Iyer, G., Weiss, S. & Enderlein, J. Fast, background-free, 3d
456 super-resolution optical fluctuation imaging (sofi). *Proc. Natl. Acad. Sci.* **106**, 22287–
457 22292, (2009).
- 458 11 Gustafsson, N. et al. Fast live-cell conventional fluorophore nanoscopy with ImageJ
459 through super-resolution radial fluctuations. *Nat. Commun.* **7**, 12471, (2016).
- 460 12 Agarwal, K. & Machán, R. Multiple signal classification algorithm for super-resolution
461 fluorescence microscopy. *Nat. Commun.* **7**, 13752, (2016).
- 462 13 Yahiatene, I., Hennig, S., Müller, M. & Huser, T. Entropy-Based Super-Resolution
463 Imaging (ESI): From Disorder to FineDetail. *ACS Photonics* **2**, 1049–1056, (2015).
- 464 14 Culley, S. et al. Quantitative mapping and minimization of super-resolution optical
465 imaging artifacts. *Nat. Methods* **15**, 263–266, (2018).
- 466 15 Fukunaga, K. & Hostetler, L. The estimation of the gradient of a density function, with
467 applications in pattern recognition. *IEEE Transactions on Inf. Theory* **21**, 32–40, (1975).
- 468 16 Yizong Cheng. Mean shift, mode seeking, and clustering. *IEEE Transactions on Pattern*
469 *Analysis Mach. Intell.* **17**, 790–799, (1995).

- 470 17 Comaniciu, D. and Meer, P., Mean shift: a robust approach toward feature space analysis,
471 IEEE Transactions on Pattern Analysis Mach. Intell. **24**, 603–619 (2002).
- 472 18 Emami, E., Fathy, M. and Kozegar, E. Online failure detection and correction for
473 camshiftracking algorithm, 2013 8th Iranian Conference on Machine Vision and Image
474 Processing (MVIP), (2013), pp. 180–183.
- 475 19 Fazekas, F. J., Shaw, T. R., Kim, S., Bogucki, R. A. & Veatch, S. L. A mean shift
476 algorithm for drift correction in localization microscopy. Preprint at
477 <https://doi.org/10.1101/2021.05.07.443176> (2021).
- 478 20 Rayleigh, L. On the theory of optical images, with special reference to the microscope. J.
479 Royal Microsc. Soc. **23**, 474–482, (1903).
- 480 21 Sparrow, C. M. On Spectroscopic Resolving Power. *Astrophys. J.* **44**, 76, (1916).
- 481 22 Diaspro, A. & Bianchini, P. Optical nanoscopy. *La Rivista del Nuovo Cimento* **43**, 385–
482 455, (2020).
- 483 23 Sharma, K. *Optics: Principles and Applications* (Academic Press, Elsevier Science, 2006).
- 484 24 Dataset: Tubulin 2d high density. <http://bigwww.epfl.ch/smlm/challenge2013/>.
- 485 25 Sage, D. et al. Super-resolution fight club: assessment of 2D and 3D single-molecule
486 localization microscopy software. *Nat. Methods* **16**, 387–395, (2019).
- 487 26 Dataset: Bundled tubes high density. <http://bigwww.epfl.ch/smlm/challenge2013/>.
- 488 27 Schnitzbauer, J., Strauss, M. T., Schlichthaerle, T., Schueder, F. & Jungmann, R. Super-
489 resolution microscopy with DNA-PAINT. *Nat. Protoc.* **12**, 1198–1228, (2017).
- 490 28 Wang, H. & Milstein, J. N. Simulation Assisted Analysis of the Intrinsic Stiffness for
491 Short DNA Molecules Imaged with Scanning Atomic Force Microscopy. *PLOS ONE* **10**,
492 1–11, (2015).
- 493 29 Corbett, A. D. et al. Microscope calibration using laser written fluorescence. *Opt. Express*
494 **26**, 21887–21899, (2018).
- 495 30 Garcés Suárez, Y. et al. Nanoscale organization of rotavirus replication machineries. *elife*
496 **8**, e42906, (2019).
- 497 31 Romarowski, A. et al. Super-resolution imaging of live sperm reveals dynamic changes of
498 the actin cytoskeleton during acrosomal exocytosis. *J. Cell Sci.* **131**, (2018).
- 499 32 Balestrini, P. A. et al. Seeing is believing: Current methods to observe sperm acrosomal
500 exocytosis in real time. *Mol. Reproduction Dev.* **87**, 1188–1198, (2020).
- 501 33 Cox, S. et al. Bayesian localization microscopy reveals nanoscale podosome dynamics.
502 *Nat. Methods* **9**, 195–200, (2012).
- 503 34 Jin, S., Haggie, P. M. & Verkman, A. S. Single particle tracking of membrane protein
504 diffusion in a potential: Simulation, detection, and application to confined diffusion of cfr
505 cl-channels. *Biophys. J.* **93**, 1079–1088, (2007).

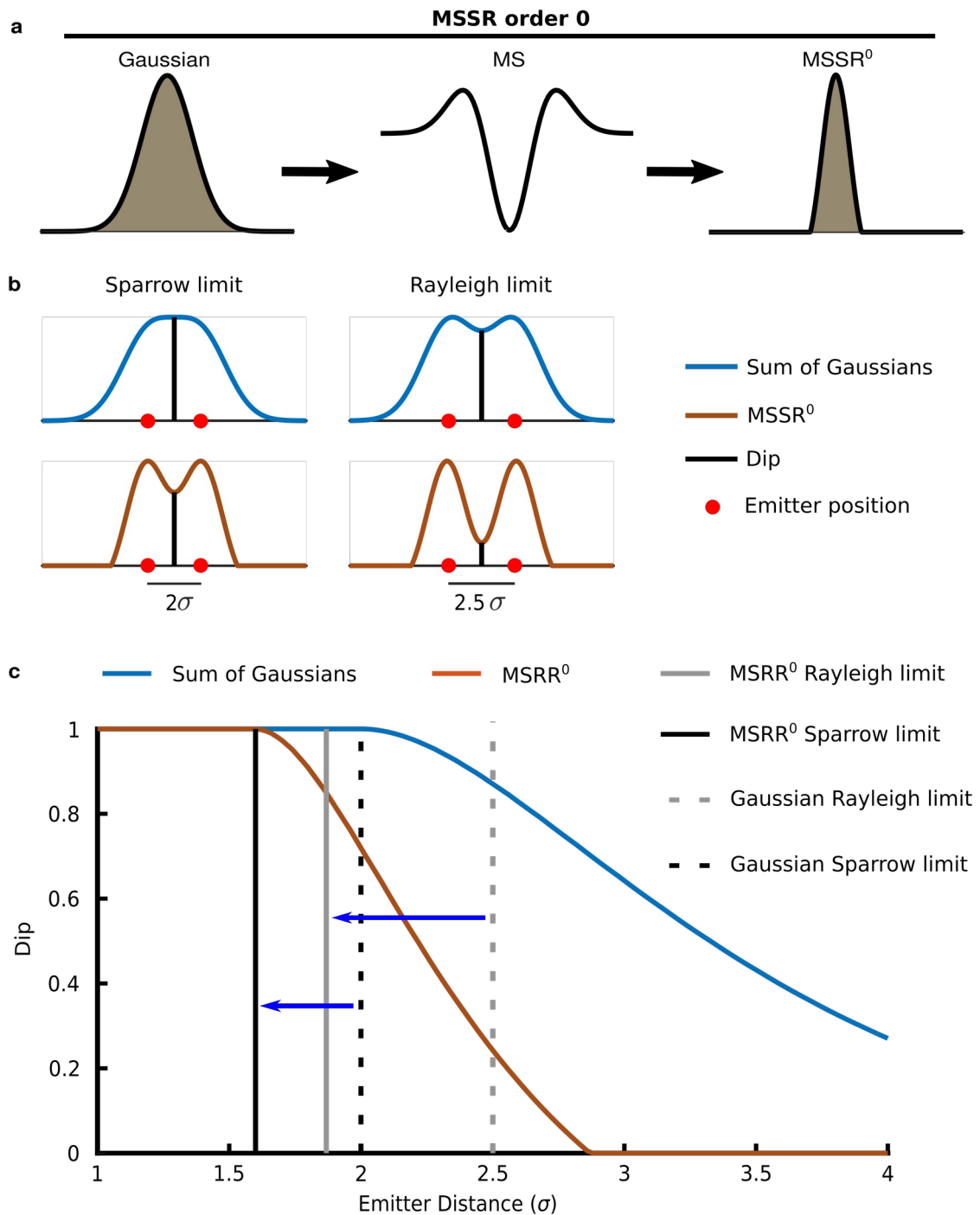
- 506 35 Yamashita, N. et al. Three-dimensional tracking of plus-tips by lattice light-sheet
507 microscopy permits the quantification of microtubule growth trajectories within the
508 mitotic apparatus. *J. Biomed. Opt.* **20**, 1 – 18, (2015)
- 509 36 Chenouard, N. et al. Objective comparison of particle tracking methods. *Nat. Methods* **11**,
510 281–289, (2014).
- 511 37 Jaqaman, K., Loerke, D., Mettlen, M., Kuwata, H., Grinstein, S., Schmid, S. L. and
512 Danuser, G. Robust single-particle tracking in live-cell time-lapse sequences, *Nat.*
513 *Methods* **5**, 695 (2008).
- 514 38 Fields, A. P. and Cohen, A. E. Optimal tracking of a brownian particle, *Opt. Express* **20**,
515 22585–22601 (2012).
- 516 39 Kalman, R. E. A New Approach to Linear Filtering and Prediction Problems, *J. Basic*
517 *Eng.* **82**, 35–45 (1960).
- 518 40 Yüce M. Y., Erdoğan, A., Jonáš, A. & Kiraz, A. Single molecule tracking with kalman
519 filtering. *Frontiers in Optics 2011/Laser Science XXVII, FTuH5*, (Optical Society of
520 America, 2011).
- 521 41 Tinevez, J.-Y., Perry, N., Schindelin, J., Hoopes, G. M., Reynolds, G. D., Laplantine, E.,
522 Bednarek, S. Y., Shorte, S. L. and Eliceiri, K. W. Trackmate: An open and extensible
523 platform for single-particle tracking, *Methods* **115**, 80–90 (2017).
- 524 42 Patel, M., Leggett, S. E., Landauer, A. K., Wong, I. Y., and Franck, C. Rapid, topology-
525 based particle tracking for high-resolution measurements of large complex 3D motion
526 fields, *Sci. Reports* **8**, 5581 (2018).
- 527 43 Gross, J., Köster, M. & Krüger, A. Fast and efficient nearest neighbor search for particle
528 simulations. *Computer Graphics and Visual Computing CGVC*, 55–63, (The
529 Eurographics Association, 2019).
- 530 44 Cheezum, M. K., Walker, W. F., and Guilford, W. H. Quantitative Comparison of
531 Algorithms for Tracking Single Fluorescent Particles, *Biophys. J.* **81**, 2378–2388 (2001).
- 532 45 Calcines-Cruz, C., Finkelstein, I. J. & Hernandez-Garcia, A. Crispr-guided programmable
533 self-assembly of artificial virus-like nucleocapsids. *Nano Lett.* **21**, 2752–2757, (2021).
- 534 46 Federici, F., Dupuy, L., Laplaze, L., Heisler, M. & Haseloff, J. Integrated genetic and
535 computation methods for *in planta* cytometry. *Nat. Methods* **9**, 483–485, (2012).
- 536 47 Torres-Martínez, H. H., Hernández-Herrera, P., Corkidi, G. & Dubrovsky, J. G. From one
537 cell to many: Morphogenetic field of lateral root founder cells in *arabidopsis thaliana* is
538 built by gradual recruitment. *Proc. Natl. Acad. Sci.* **117**, 20943–20949, (2020).
- 539 48 Ricci, M. A., Manzo, C., García-Parajo, M. F., Lakadamyali, M., & Cosma, M. P. (2015).
540 Chromatin fibers are formed by heterogeneous groups of nucleosomes in vivo. *Cell*, **160**,
541 1145-1158.

- 542 49 Rutowicz, K., Lirski, M., Mermaz, B., Teano, G., Schubert, J., Mestiri, I., Kroten, M., A.,
543 Fabrice, T. N., Fritz, S., Grob, S., Ringli, C., Cherkezyan, L., Barneche, F., Jerzmanowski,
544 A., and Baroux, C. Linker histones are fine-scale chromatin architects modulating
545 developmental decisions in arabidopsis, *Genome Biol.* **20**, 157 (2019).
- 546 50 Wu, G., Zhao, X., Luo, S. & Shi, H. Histological image segmentation using fast mean
547 shift clustering method. *BioMedical Eng. OnLine* **14**, 24, (2015).
- 548 51 Szeliski, R. *Computer vision: Algorithms and applications* (Springer Science & Business
549 Media, 2011).
- 550 52 Sankaran, J. et al. Simultaneous spatiotemporal super-resolution and multi-parametric
551 fluorescence microscopy. *Nat. Commun.* **12**, 1748, (2021).
- 552 53 Lin, Y.-H., Chang, W.-L., and Hsieh, C.-L. Shot-noise limited localization of single 20
553 nm gold particles with nanometer spatial precision within microseconds, *Opt. Express* **22**,
554 9159–9170 (2014).
- 555 54 Glover, Z. J., Ersch, C., Andersen, U., Holmes, M. J., Povey, M. J., Brewer, J. R. and
556 Simonsen, A. C. Super-resolution microscopy and empirically validated autocorrelation
557 image analysis discriminates microstructures of dairy derived gels,” *Food Hydrocoll.* **90**,
558 62–71(2019).
- 559 55 Betzig, E. Nobel lecture: Single molecules, cells, and super-resolution optics, *Rev. Mod.*
560 *Phys.* **87**, 1153–1168 (2015).
- 561 56 Liss, V., Barlag, B., Nietschke, M. and Hensel, M. Self-labelling enzymes as universal
562 tags for fluorescence microscopy, super-resolution microscopy and electron microscopy,
563 *Sci. Reports* **5**, 17740 (2015).
- 564 57 de Boer, P., Hoogenboom, J. P. & Giepmans, B. N. G. Correlated light and electron
565 microscopy: ultrastructure lights up! *Nat. Methods* **12**, 503–513, (2015).
- 566 58 Cahoon, C. K. et al. Superresolution expansion microscopy reveals the three-dimensional
567 organization of the Drosophila synaptonemal complex. *Proc. Natl. Acad. Sci.* **114**, 6857–
568 6866, (2017).
- 569 59 Kim, J., Wojcik, M., Wang, Y., Moon, S., Zin, E.A., Marnani, N., Newman, Z.L.,
570 Flannery, J.G., Xu, K. and Zhang, X. Oblique-plane single-molecule localization
571 microscopy for tissues and small intact animals, *Nat. Methods* **16**, 853–857 (2019).
- 572 60 Hu, Y. S., Zimmerley, M., Li, Y., Watters, R. and Cang, H. Single-molecule super-
573 resolution light-sheet microscopy,” *ChemPhysChem* **15**, 577–586 (2014).
- 574 61 Chen, R., Tang, X., Shen, Z., Shen, Y., Li, T., Wang, J., Cui, B., Guo, Y., Du, S. and Yao,
575 S. Deep-learning super-resolution microscopy reveals nanometer-scale intracellular
576 dynamics at the millisecond temporal resolution, Preprint at
577 <https://doi.org/10.1101/2021.10.08.463746> (2021).

- 578 62 Puschmann, K. G. & Kneer, F. On super-resolution in astronomical imaging. *Astronomy*
579 & *Astrophysics* **436**, 373–378, (2005).
- 580 63 Guo, R., Shi, X., Zhu, Y. & Yu, T. Super-resolution reconstruction of astronomical
581 images using time-scale adaptive normalized convolution. *Chin. J. Aeronaut* **31**, 1752–
582 1763, (2018).

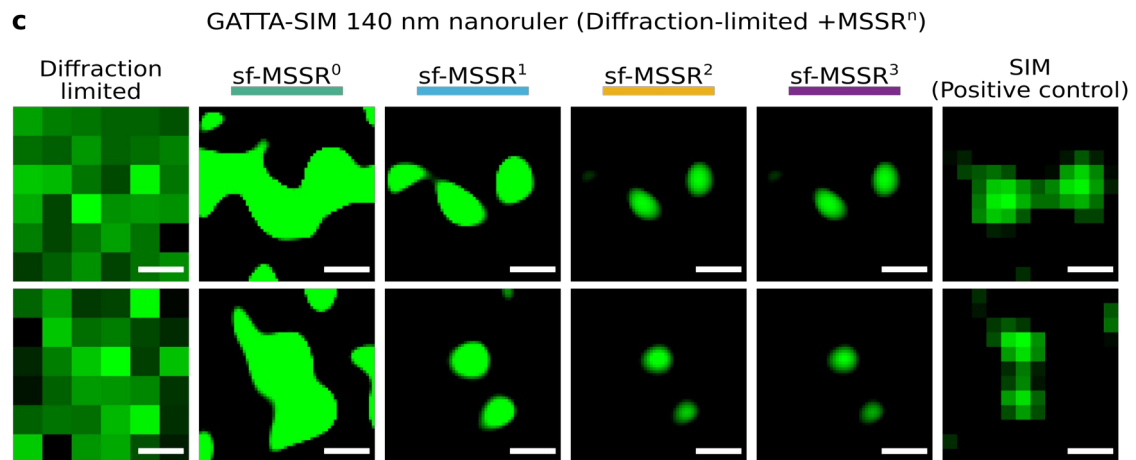
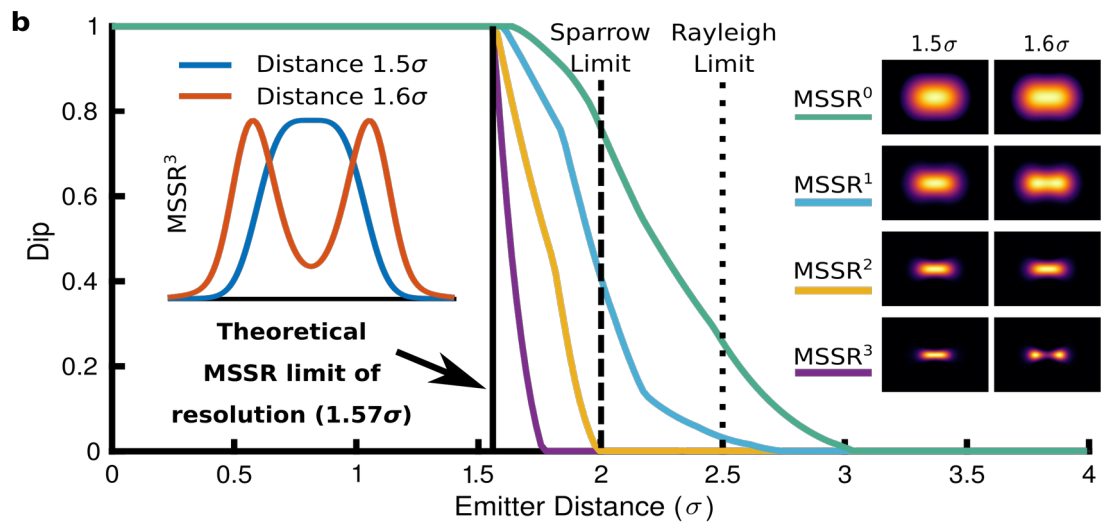
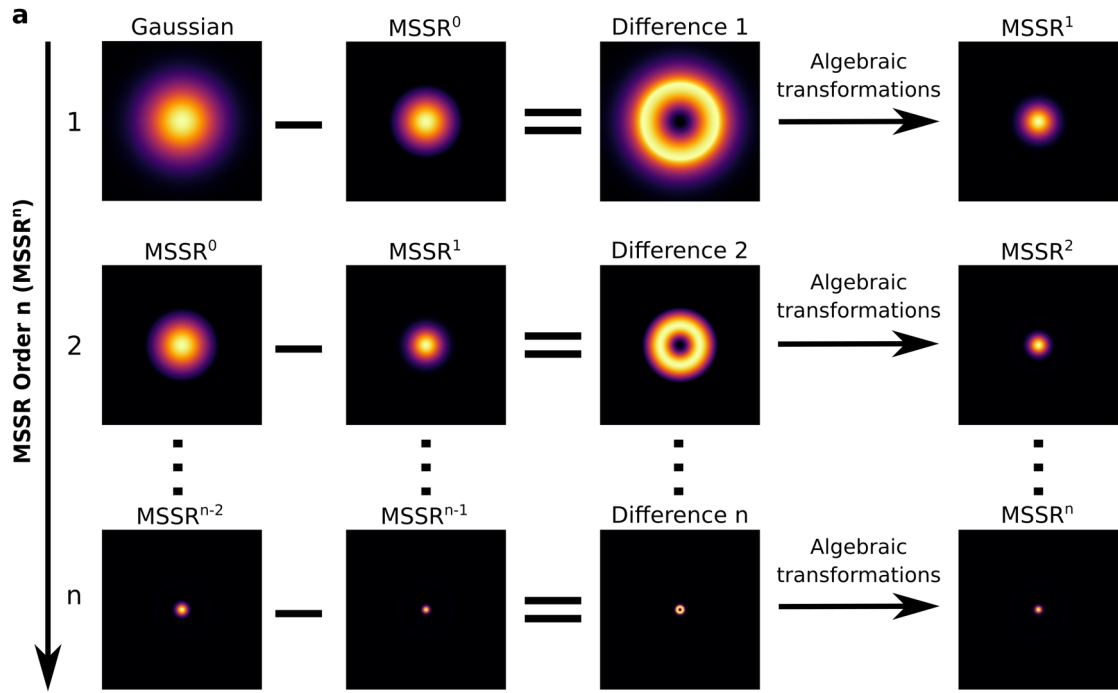
583 **Figures**

584



586 **Figure 1. MSSR of zero order increases resolution by reducing the width of the**
 587 **spatial distribution of photons emitted from modelled fluorescent emitters. a)** The
 588 MS is applied to the initial Gaussian distribution of photons emitted by a point-source
 589 (left) resulting in a MS graph (center). Application of further algebraic transformations

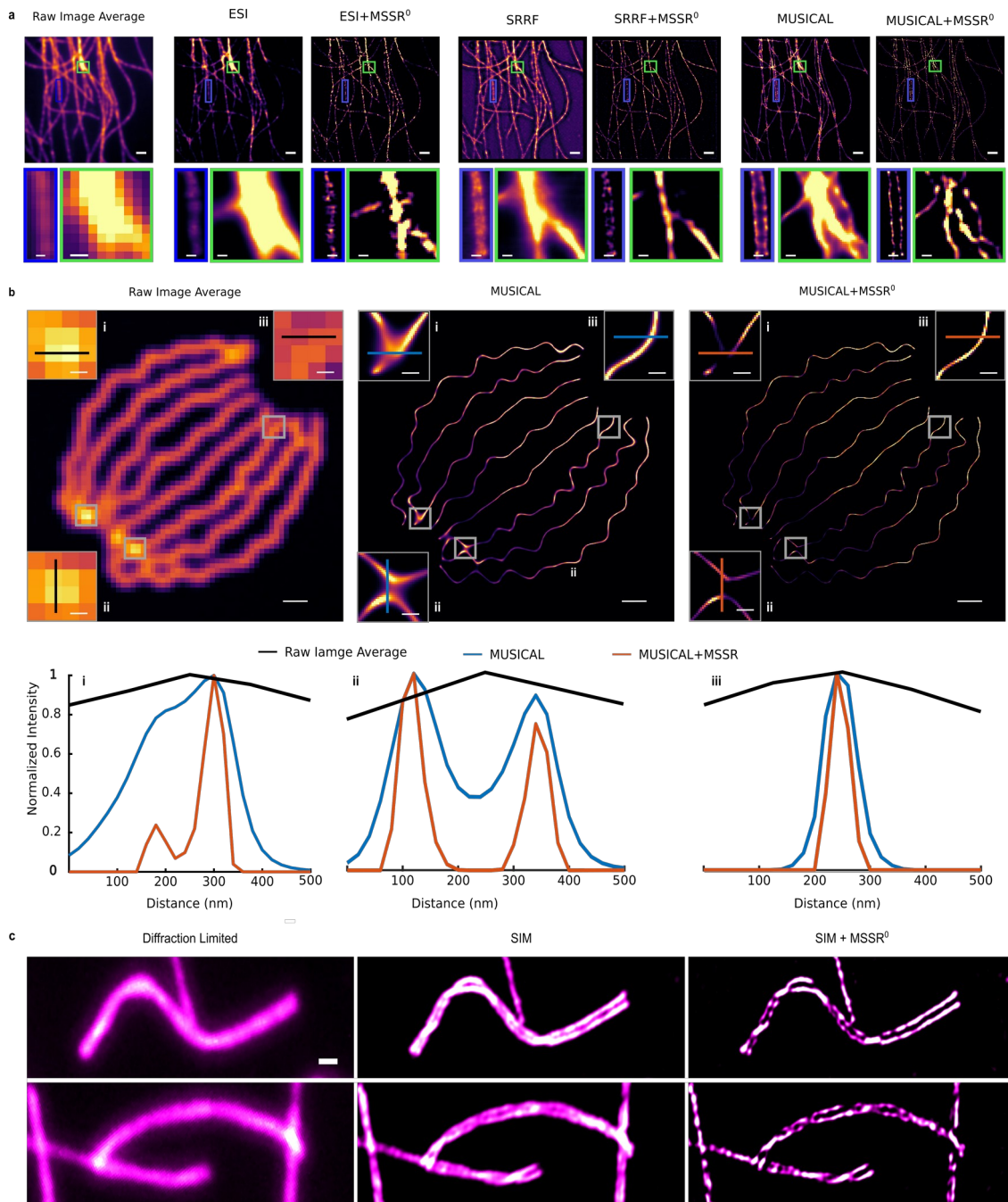
590 (see Supplementary Note 5 and Figure S7 (ii-iv)) provides the $MSSR^0$ distribution
591 (right). **b)** Sparrow and Rayleigh limits (blue, diffraction-limited) and the corresponding
592 $MSSR^0$ transformation (brown) for two point-sources. Red dots represent each emitter's
593 location. The dip is indicated by a vertical black line. The inter-emitter distance is
594 expressed as σ -times their individual standard deviation before $MSSR$ processing. **c)**
595 Dip computed for two point-source emitters of Gaussian distribution located away at
596 distinct σ (blue line) where the corresponding $MSSR^0$ result is also depicted (red line).
597 For Gaussian: Rayleigh limit – gray discontinuous line, Sparrow limit - black
598 discontinuous line. For $MSSR^0$: Rayleigh limit - gray solid line, Sparrow limit - gray
599 solid line. The solid vertical lines represent the distance between emitters such that
600 when processed with $MSSR^0$, the criteria of Rayleigh and Sparrow are obtained.
601



603 **Figure 2. Single-frame MSSR analysis of higher order attains a resolution limit of**
604 **1.6 σ for nearby emitters. a)** The algorithm for computing higher-order MSSR
605 (MSSRⁿ) is presented. The first iteration of MSSR (MSSR¹) is given by subtracting the
606 MSSR⁰ from the original image, resulting in a donut-like region centered at the
607 emitter's location. MSSR¹ is computed after applying further algebraic transformations
608 (see Supplementary Note 5 and Figure S8 (ii-iv) for a full description of the MSSRⁿ
609 process). The second iteration encompasses the subtraction of MSSR¹ from MSSR⁰ and
610 the same algebraic transformations as used for generation of MSSR¹. The process is
611 repeated by updating consecutive MSSR images which generates higher MSSR orders.
612 **b)** Theoretical limit of resolution achievable by MSSRⁿ. Dip computed for two Gaussian
613 emitters in accordance with the variation of the inter-emitter distance (expressed as σ -
614 times their standard deviation before MSSR processing). Colored lines represent the dip
615 of MSSR order, from 0 to 3, computed at a given σ distance between emitters. Images
616 on the right are the bidimensional representation of the MSSRⁿ processing for two
617 single emitters separated at distances of 1.5σ and 1.6σ . Note that, for 1.5σ , emitters are
618 unresolved up to the third order of MSSR. **c)** Experimental demonstration of the
619 resolution increases attainable with higher order MSSR using the GATTA-SIM 140B
620 nanoruler system. The intensity distribution of the emitter shrinks, both in σ and
621 intensity, as the order of the MSSR increases (Figure S8). Nearby emitters (Alexa
622 Fluor® 488) located 140 nm apart are resolved using MSSR¹, MSSR² and MSSR³ (right
623 side). SIM images collected from the same sample (distinct fields) are shown as a
624 positive control. Scale bar: 100 nm.

625

626

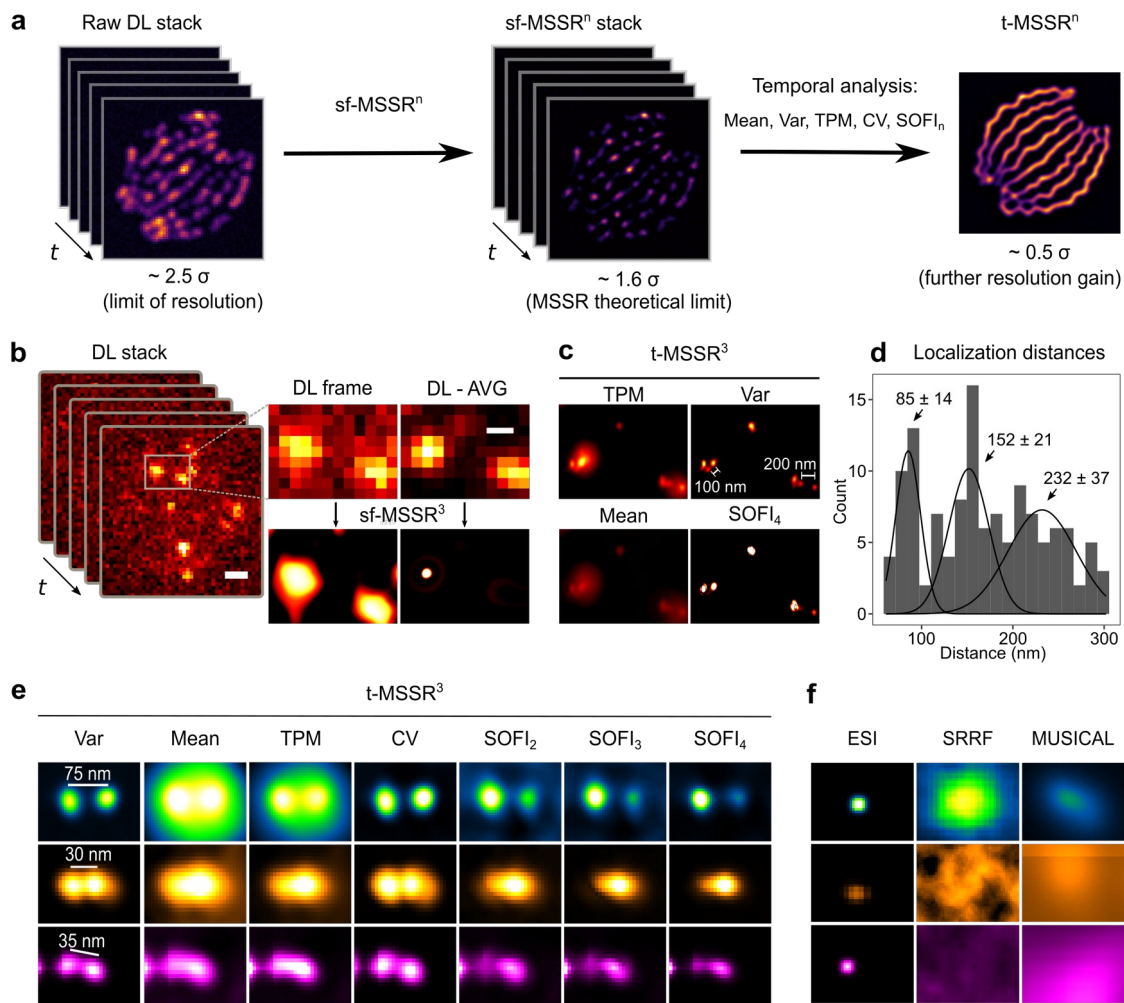


628 **Figure 3. MSSR enhances resolution and contrast of single super-resolved images.**
 629 **a)** Comparison of SRM results of ESI, SRRF and MUSICAL alone and after post-
 630 processing with MSSR⁰ (ESI + MSSR⁰, SRRF + MSSR⁰, MUSICAL + MSSR⁰), over a
 631 temporal stack of 500 DL images of tubulin-labeled microtubules. The average
 632 projection of the DL stack is shown on the leftmost side. **b)** Comparison of the increase
 633 in spatial resolution of MUSICAL with and without post-processing with MSSR⁰
 634 (MUSICAL + MSSR⁰), over a temporal stack of 361 DL images of modelled
 635 fluorophores bounded to a synthetic array of nanotubules (average projection shown on

636 left). The graphs show the intensity profiles along the lines depicted in each of the insets
637 in the images of the upper row; black, blue and red lines correspond to the average DL,
638 MUSICAL and MUSICAL + MSSR⁰ images, respectively. **c)** Sister chromatids of
639 mitotic mouse chromosomes visualized by TIRFM (left), SIM (middle) and SIM +
640 MSSR⁰ (right). Scale bars: **a)** 1 μm , insets = 200 nm; **b)** 500 nm, insets = 100 nm; **c)**
641 200 nm.

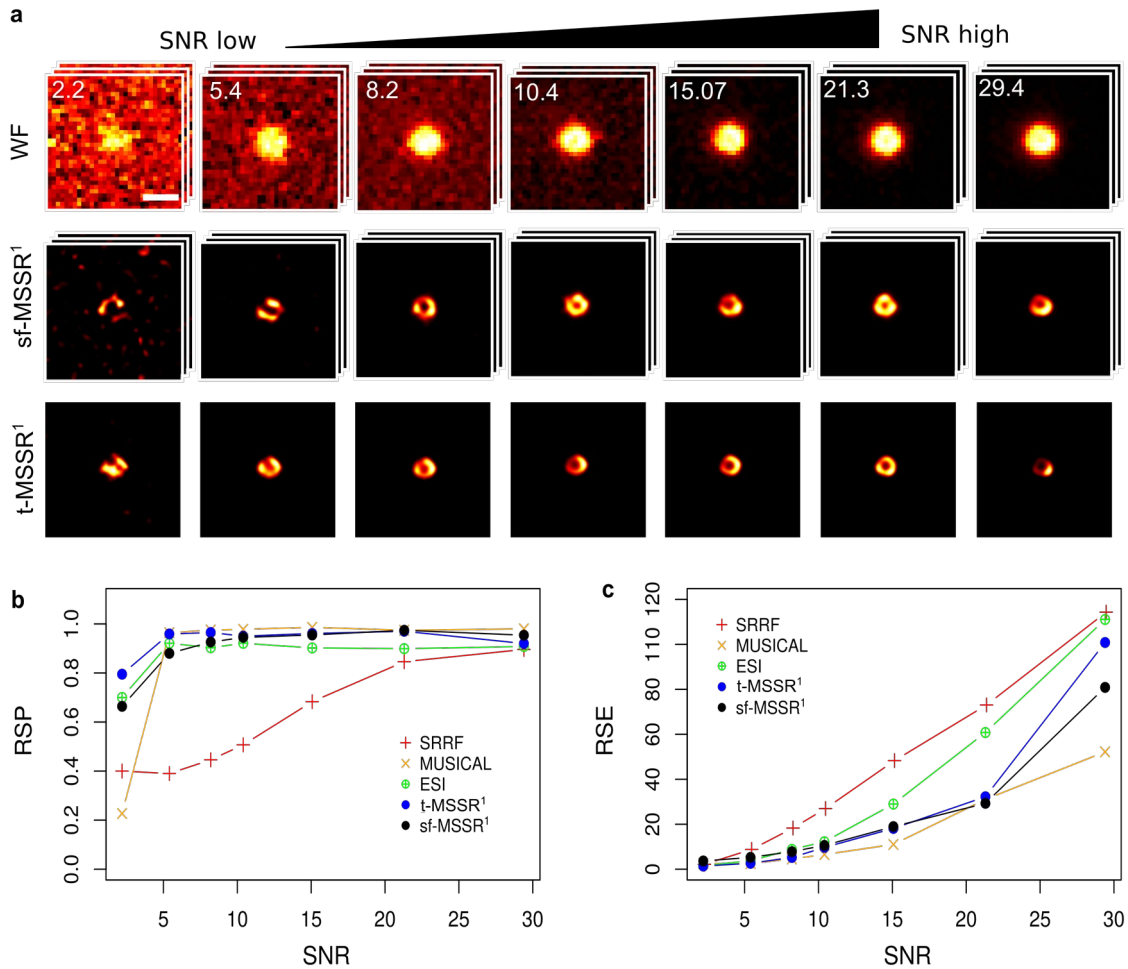
642

643



645 **Figure 4. The temporal analysis of MSSR provides a further increase in resolution**
 646 **to approximately 40 nm. a)** Single-frame analysis of MSSR of a given order n is
 647 applied to each frame of a sequence, becoming the sf-MSSR n stack. Next, a pixel-wise
 648 temporal function (PTF) converts the MSSR stack into a single super-resolved t-MSSR n
 649 image. Depending on the temporal entropy of the dataset and on the PTF used, a
 650 resolution enhancement can be obtained. **b)** Left: a stack of DL images of a
 651 CRISPR/dCas12a nanoruler system. Scale bar: 1 μm . Right: zoomed region of the first
 652 frame in the stack, along with the average projection (DL-AVG) of a stack of 100
 653 images, before and after MSSR processing. Scale bar: 400 nm. **c)** PTF applied to a stack
 654 of MSSR 3 images (t-MSSR 3). Fluorescent emitters are separated by 100 nm, as
 655 established by the CRISPR/dCas12a nanoruler system. Four types of PTF were
 656 computed: *TPM*, *Var*, *Mean* and *SOFI $_4$* . **d)** Euclidean distances between nearby emitters
 657 automatically computed from t-MSSR 3 -*Var* images, following a worm-like chain model

658 (16 regions of interest used, 1.5 μm^2 each). **e)** Comparison of the results obtained with
659 each of the PTF analysis available with MSSR (see Table S3), for a commercially
660 available GATTA-PAINT nanoruler system. The *Var* column shows inter-emitter
661 distances resolved in the range 30 –75 nm. Atto 488 (green), Atto 550 (orange) and Atto
662 655 (magenta) fluorescent probes were used. **f)** Same nanorulers shown in **e)** but
663 analyzed with either ESI, SRRF or MUSICAL.



665 **Figure 5. MSSR is robust to image noise and shows high global performance when**
 666 **compared to other SRM analytical procedures. a)** sf-MSSR¹ and t-MSSR¹ of 100
 667 images provide consistent reconstructions across a wide range of SNR. The expected
 668 feature is a uniform fluorescent ring located at the center of the image with a dark
 669 background lacking fluorescence. Each image is displayed to show its full intensity
 670 range. The row for DL images (Widefield, WF) exemplifies a stack of 100 frames
 671 collected at the corresponding SNR. The central row represents a resolved stack using
 672 sf-MSSR¹. The third row shows the super-resolved micrography after t-MSSR¹ analysis
 673 of 100 DL images using *TPM* for temporal analysis (see table S2). Scale bar: 1 μ m. **b-c)**
 674 Resolution Scaled Pearson (RSP) coefficient (b) and Resolution Scaled Error (RSE) (c),
 675 computed for the super-resolution reconstructions provided by SRRF, MUSICAL, ESI,
 676 sf-MSSR¹ and t-MSSR¹ (100 frames). **b)** RSP measures a global correlation between
 677 reconstruction and reference (input DL image), values closer to 1 indicate a reliable
 678 reconstruction. **c)** RSE measures the absolute difference of the reconstructed image and

679 its reference. Lower values of RSE at a particular SNR mean reduced global error in the
680 reconstruction. Scale bar: 1 μm .

681

682 **Data availability**

683 All raw imaging data which support the findings of this study are available from the
684 corresponding author upon request. Source data are provided with this paper.

685 Correspondence and requests for materials should be addressed to A.G.

686

687 **Code availability**

688 Source code for R and MATLAB platforms is available as supplementary materials, the
689 MSSR plugin for FIJI/ImageJ is available at <https://github.com/MSSRSupport/MSSR>.

690

691 **Funding**

692 This research was supported by Dirección General de Asuntos del Personal Académico
693 (DGAPA) – Programa de Apoyo a Proyectos de Investigación e Innovación

694 Tecnológica-UNAM (PAPIIT). and by Mexican Consejo Nacional de Ciencia y

695 Tecnología (CONACyT) grant A1-S-9236 to JGD, grant number IN211821 to AG,

696 IN211216 to CDW, IN204221 to JGD. Microscopy equipment was provided and

697 maintained through CONACYT grants 123007, 232708, 260541, 280487, 293624 and

698 294781. MB thank to IBYME-CONICET: Grants: PICT 2017-3047 (Agencia Nacional

699 de Promoción de la Investigación, el Desarrollo Tecnológico y la Innovación),

700 Fundación Williams; Fundación Rene Barón. DK acknowledges the support of the

701 National Science Foundation grant 2102832.

702 We also acknowledge the Programa de Becas de Posgrado of CONACYT for

703 granting scholarships to ETG, RPC, AL, DM, VA, EBA, CCC, GVG, DT, HTM, JLM,

704 HH, and to JPO. YG acknowledges DGAPA/UNAM for postdoctoral fellowship.

705

706 **Acknowledgements**

707 To the Microscopy Facility at EMBL Rome and IBYME-CONICET for providing

708 samples and materials for experiments. To the ECE and ICIMAF institutes for

709 theoretical and experimental input to this work. The authors thank the LNMA staff for

710 providing support with microscopy imaging. The OpenSPIM project was technically
711 executed and extended by Oliver Valdez Escalona. ET and AG thank Angelica Flores
712 Navarrete and Yuriney Abonza Amaro for their valuable feedback during the
713 elaboration of the manuscript.

714

715 **Author contributions**

716 Conceptualization: ET, AG.

717 Methodology: ET, AG, RP, AHC, RR., JGD.

718 Investigation: ET, AG, RP, AHC, DM, VA, EBA, CC, GV, AHG, DT, JM, YG, MaB,
719 MJ, HTM, HH, JO.

720 Visualization: ET, AG, HT.

721 Supervision: AG, AHC, DK.

722 Funding Acquisition: AG, AD, MB, JGD, CW.

723 Project Administration: AG.

724 Drafting Main Document: ET, AG, AL, AHC, CW.

725 Drafting Supplementary Material: ET, AG, AL, RR, JR, DK.

726 All authors contributed to the writing and reviewing of the manuscript.

727

728 **Competing interests**

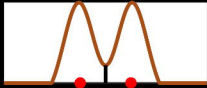
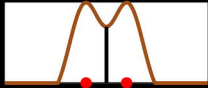
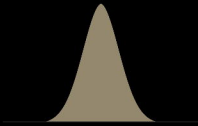
729 The authors declare no competing interests.

730

731 **Additional information**

732 The online version contains supplementary methods, supplementary notes,
733 supplementary movies, the MSSR manual for FIJI/ImageJ, MSSR scripts R and
734 MATLAB, and additional references.

735



σ

σ

